

**Citation for published version:**

Qiwu Luo, Yigang He, and Yichuang Sun, "Real-Time Fault Detection and Diagnosis System for Analog and Mixed-signal Circuits of Acousto-Magnetic EAS Devices", *IEEE Design and Test*, Vol. 33 (3), September 2015.

**DOI:**

[10.1109/MDAT.2015.2480714](https://doi.org/10.1109/MDAT.2015.2480714)

**Document Version:**

This is the Accepted Manuscript version.

The version in the University of Hertfordshire Research Archive may differ from the final published version. **Users should always cite the published version of record.**

**Copyright and Reuse:**

© 2015 IEEE.

Personal use of this material is permitted. Permission from IEEE must be obtained for all other uses, in any current or future media, including reprinting/republishing this material for advertising or promotional purposes, creating new collective works, for resale or redistribution to servers or lists, or reuse of any copyrighted component of this work in other works.

**Enquiries**

If you believe this document infringes copyright, please contact the Research & Scholarly Communications Team at [rsc@herts.ac.uk](mailto:rsc@herts.ac.uk)

# Real-Time Fault Detection and Diagnosis System for Analog and Mixed-signal Circuits of Acousto-Magnetic EAS Devices

Qiwu Luo, Yigang He, Yichuang Sun, *Senior Member, IEEE*

**Abstract**—Real-time fault detection and diagnosis of analog and mixed-signal circuits are challenging due to the large-scale integration and component tolerance. This paper presents a modular fault diagnostic system based on FPGA. Rather than dealing with the whole circuit directly, the proposed approach partitions a large-scale circuit into several small sub-circuits according to the circuit nature or signal flow and handles each sub-circuit by using two-dimensional information fusion, network analysis, and interval math theory. In the real applications of acousto-magnetic EAS products, two test examples are given to demonstrate the diagnosis performance for both pure analog and mixed-signal circuits. Results show the method's high speed, effectiveness, and robustness.

**Index Terms**—Fault diagnosis, analog and mix-signal (AMS), circuit under test (CUT), field-programmable gate array (FPGA), electronic article surveillance (EAS)

## I. INTRODUCTION

FROM conventional fault dictionary, parameter identification and fault verification techniques to recent neural network [1], fuzzy theory [2] and wavelet analysis [3] methods, the past five decades have witnessed an unprecedented development in the field of analog fault detection and diagnosis (AFDD) especially for the study of fundamental theory. And these sustainable theoretical achievements will be gradually applied to real world engineering to realize their contributions. In [4], a fast transient testing methodology for predicting the performance parameters of analog circuits was proposed, focusing mainly on analog ICs. Moreover, a remote AFDD method was developed based on LabVIEW in [5], its diagnosis results could be monitored on web browser. These studies show invariably that diagnosis speed and test cost should be emphasized simultaneously in the testing and diagnosis of analog and mixed-signal (AMS) circuits.

This work was supported by the National Natural Science Funds of China for Distinguished Young Scholar under Grant No. 50925727, The National Defense Advanced Research Project Grant No.C1120110004 and 9140A27020211DZ5102, Hunan Provincial Science and Technology Foundation of China under Grant No.2010J4 and 2011JK2023, the Key Grant Project of Chinese Ministry of Education under Grant No.313018.

Q. Luo is with the College of Electrical and Information Engineering, Hunan University, Changsha 410082, China (e-mail: [luoqiwu@hnu.edu.com](mailto:luoqiwu@hnu.edu.com)).

Y. He is with the School of Electrical and Automation Engineering, Hefei University of Technology, Anhui, China (e-mail: [18655136887@163.com](mailto:18655136887@163.com)).

Y. Sun is with the School of Engineering and Technology, University of Hertfordshire, Hatfield AL10 9AB, U.K. (e-mail: [y.sun@herts.ac.uk](mailto:y.sun@herts.ac.uk)).

Electronic article surveillance (EAS) detection devices are used to evaluate human exposure to designated electromagnetic fields [6]. Although the RFID technology has been revealing its ambition in expanding its range of application, the acousto-magnetic (AM) technology due to owning more reliable performance is dominating today's EAS industry. The normal operating of EAS systems are directly linked to the economic benefits both in the apparel industry and in retail. Until 2012, although retailers had introduced EAS technologies, around 25% of the most-stolen products still had no specific protections [7], needless to say that when the equipped EAS systems are off-normal. For a general AM-EAS detection system, the electronic control board (ECB), being the most vital constituent part, is a typical large-scale AMS circuit. And these kinds of soldered printed circuit board (PCB) are continuously operating in EAS equipments to support the non-stop profit protection by reducing shoplifting, theft and vendor fraud. However at present, the common handling method on the faulty ECBs is to replace them with brand-new ones by their suppliers, and then diagnose the possible faults offline. Such solutions have caused economic and time losses to both EAS device suppliers and retailers.

On the other hand, FPGA is by far parallel and highly reconfigurable, permitting rapid prototyping of control mechanisms and new algorithms for pre-research and realistic applications. These advantages show an opportunity to set up practical AFDD systems for the AM-EAS devices. In the recent past, FPGA has been widely applied for real-time power converter failure diagnosis, vibration analyses for industrial applications, and ionizing radiation detection for environmental awareness among many others. However, to our knowledge, FPGA-based real-time analog circuit diagnosis for AM-EAS products has not been available.

This paper mainly extends our previous diagnosis method by fusing information of gain-frequency and node voltages [8, 9]. Considering that the circuit accessible node voltages, responses of amplitude-frequency (A-F) and phase-frequency (P-F) contain abundant fault information, a FPGA-centered fault diagnosis prototype based on the above mentioned three circuit features is developed. The interval-math-based diagnosis algorithm is then tested on the realized prototype.

The structure of the paper is as follows. Section II focuses on fault diagnosis theory, including how to extract the A-F and P-F parameters in real time. Following the theory, Section III presents the hardware topology of the diagnosis prototype and some key implementation details are described as well. Two experimental cases and their test results are shown in Section IV and Section V to prove the effectiveness of the proposed method. And finally, Section VI gives our conclusions and ideas for future work.

## II. FEATURE EXTRACTION AND DIAGNOSIS THEORY

This section firstly introduces our circuit fault feature extraction method, and the orthogonal algorithm which is conducive to FPGA realization is also presented in detail. Then the diagnosis methods and judging rules using the techniques of interval math and information fusion are presented.

### A. Approaches of Amplitude and Phase Detection

Many recent publications show that the node-voltage-based diagnostic methods are becoming increasingly mature [9]. Hence we only describe the real-time data acquisition approach of the A-F and P-F characteristics to avoid cumbersome.

Digital amplitude and phase discriminations are extensively applied in intermediate frequency domain, which means it is practicable to adopt digital analysis approaches to fault diagnosis of large-scale AMS circuits. The data acquisition scheme is shown in Fig. 1. In order to diagnose the potential failure, we partition the whole small-signal-processing circuit into several small sub-networks according to the signal flow.

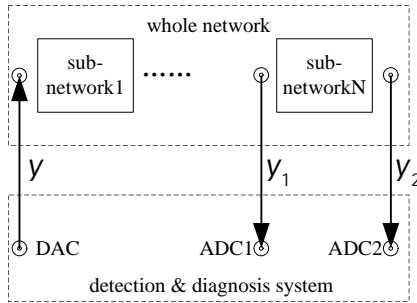


Fig. 1. Testing diagram for analog network.

Supposing that the excitation signal on the DAC terminal is defined as  $y = \sin(\omega t)$ , the input and output signals of a certain sub-network are respectively expressed as  $y_1(t) = A_1 \sin(\omega t + \phi)$  and  $y_2(t) = A_2 \sin(\omega t + \theta)$ , which are fed back into the fault detecting system via ADC1 and ADC2 ports. Then the amplitude, phase and network gain can be calculated according to (1)-(7) using orthogonal algorithm.

$$\begin{aligned} k_{11} &= \sum_{n=0}^{H-1} y_1\left(\frac{nT}{H}\right) \times \cos\left(\frac{\omega nT}{H}\right) \\ &= \sum_{n=0}^{H-1} \left( \frac{1}{2} A_1 \sin\left(\frac{2\omega nT}{H} + \phi\right) + \frac{1}{2} A_2 \sin \phi \right) = \frac{H}{2} A_1 \sin \phi \end{aligned} \quad (1)$$

$$\begin{aligned} k_{12} &= \sum_{n=0}^{H-1} y_1\left(\frac{nT}{H}\right) \times \sin\left(\frac{\omega nT}{H}\right) \\ &= \sum_{n=0}^{H-1} \left( \frac{1}{2} A_1 \cos \phi - \frac{1}{2} A_2 \cos\left(\frac{2\omega nT}{H} + \phi\right) \right) = \frac{H}{2} A_1 \cos \phi \end{aligned} \quad (2)$$

$$\begin{aligned} k_{21} &= \sum_{n=0}^{H-1} y_2\left(\frac{nT}{H}\right) \times \cos\left(\frac{\omega nT}{H}\right) \\ &= \sum_{n=0}^{H-1} \left( \frac{1}{2} A_2 \sin\left(\frac{\omega nT}{H} + q\right) + \frac{1}{2} A_2 \sin q \right) = \frac{H}{2} A_2 \sin q \end{aligned} \quad (3)$$

$$\begin{aligned} k_{22} &= \sum_{n=0}^{H-1} y_2\left(\frac{nT}{H}\right) \times \sin\left(\frac{\omega nT}{H}\right) \\ &= \sum_{n=0}^{H-1} \left( \frac{1}{2} A_2 \cos q - \frac{1}{2} A_2 \cos\left(\frac{2\omega nT}{H} + q\right) \right) = \frac{H}{2} A_2 \cos q \end{aligned} \quad (4)$$

$$\begin{cases} (1)/(2) \Rightarrow \phi = \arctan(k_{11}/k_{12}) \\ (1)^2 + (2)^2 \Rightarrow A_1 = (2/H) \sqrt{k_{11}^2 + k_{12}^2} \end{cases} \quad (5)$$

$$\begin{cases} (3)/(4) \Rightarrow q = \arctan(k_{21}/k_{22}) \\ (3)^2 + (4)^2 \Rightarrow A_2 = (2/H) \sqrt{k_{21}^2 + k_{22}^2} \end{cases} \quad (6)$$

$$\text{Network}_{\text{gain}} = A_2/A_1 \quad (7)$$

where  $k_{11}$  and  $k_{12}$  are the intermediate variables derived from  $y_1(t)$  and  $y$ , while  $k_{21}$  and  $k_{22}$  are the intermediate variables derived from  $y_2(t)$  and  $y$ ,  $T$  is the period of excitation signal,  $H$  is its quantization number per single period after discretization.

Because AM-EAS detection devices avoid item shrinkage of retail sales basically via magnetically-coupled resonant circuits tuned at a defined central frequency with an assigned bandwidth, usually 57.8 kHz ~ 58.2 kHz, the receiver sub-networks are handling these 2- amplitude shift keying (2-ASK) signals to identify whether the item under monitoring is already-paid or stolen. Unlike the narrow bandwidth of AM-EAS tags, the overall bandwidth of the receiver circuits is set to 5 kHz to maintain necessary margin for potential frequency deviation. Correspondingly during the implementation, the frequency of the excitation signal  $y$  is scanned with a pre-configured step within the 5 kHz bandwidth, the A-F and P-F parameters can then be obtained from (5) ~ (7), which constitute the fault feature vectors together with the accessible node voltages.

### B. Theory of Fault Diagnosis

#### a) Parameter selection of the feature interval

As hard fault is a special case of soft fault, thus, we treat all fault modes as soft fault type. The three parameters of node voltages, A-F and P-F characteristics form the circuit feature vector (FV) in (8).

$$\text{FV} = [f_{n_1}, \mathbf{L}, f_{n_{N1}}, f_{a_1}, \mathbf{L}, f_{a_{N2}}, f_{p_1}, \mathbf{L}, f_{p_{N3}}] \quad (8)$$

where,  $fn$ ,  $fa$ ,  $fp$  represent the features of node voltage, A-F and P-F respectively,  $N1$ ,  $N2$ ,  $N3$  are their relevant totalities. For simplifying the derivation, here we define  $N$  as the sum of them, hence we can rewrite (8) as

$$\text{FV} = [f_1, f_2, \mathbf{L}, f_N] \quad (9)$$

where  $f_j$  ( $j=1, \dots, N$ ) is the  $j^{\text{th}}$  circuit parameter of the feature vector. Then we suppose there are  $M$  circuit modes

including faulty and normal ones, then the feature interval vectors can be defined as

$$FI_i = [(L_{i1}, R_{i1}), (L_{i2}, R_{i2}), \dots, (L_{iN}, R_{iN})], i = 1, \dots, M \quad (10)$$

where  $L_{ij}$ ,  $R_{ij}$  are respectively the lower and upper bound of the  $j^{\text{th}}$  circuit parameter of the  $i^{\text{th}}$  circuit mode. The feature interval reflects the circuit mode to some degree as it is composed by the circuit parameter intervals, which can be simulated by PSpice with Monte-Carlo method.

*b) Circuit similarity of test sample to the feature interval vectors*

The feature interval represents the circuit mode so that the circuit mode could be identified by calculating the correlation degree of the test sample to the feature interval vectors. According to the fuzzy pattern recognition theory, membership degree reflects the correlation of the test sample to the mode feature vector. Referring to this relationship, the circuit similarity is selected to depict the correlation of the sample and the feature interval vectors, which is defined as follows.

Suppose that the test sample ( $TS$ ) is expressed by (11).

$$TS = [ts_1, ts_2, \dots, ts_N] \quad (11)$$

then,  $\varepsilon_{ij}$ , namely “interval similarity” of the test sample  $TS$  to the feature interval  $(L_{ij}, R_{ij})$  can be defined as

$$e_{ij} = \begin{cases} 1, (i, j) \in I \\ 1 - \frac{h_{ij}}{\sum_{i=1}^M h_{ij}}, (i, j) \notin I \end{cases} \quad (12)$$

In (12),  $I = \{(i, j) | L_{ij} \leq ts_j \leq R_{ij}, i=1, \dots, M, j=1, \dots, N\}$ , and  $h_{ij}$  is the so-called “interval relative distance” of  $TS$  to the feature interval  $(L_{ij}, R_{ij})$ , which can be expressed as (13), where  $\min$  represents the minimum value in its  $\{ \}$ .

$$h_{ij} = \frac{\min \{ |TS_j - L_{ij}|, |TS_j - R_{ij}| \}}{|L_{ij} - R_{ij}|}, j = 1, \dots, N \quad (13)$$

The nearer the  $ts_j$  is to either boundary of the feature interval  $(L_{ij}, R_{ij})$ , the wider the feature interval, the shorter the interval relative distance  $h_{ij}$  and the larger the interval similarity  $\varepsilon_{ij}$  (but less than 1). Only when  $L_{ij} \leq ts_j \leq R_{ij}$ , then  $\varepsilon_{ij}$  reaches 1. Furthermore,

$$e_i = \frac{1}{N} \sum_{j=1}^N e_{ij}, i = 1, \dots, M \quad (14)$$

$\varepsilon_i$  represents the average circuit similarity of the  $TS$  to the  $i^{\text{th}}$  feature interval vector under information fusion of  $N$  circuit parameters.

*c) Diagnosis rules using information fusion*

The responses of the tolerance circuit under different modes are sometimes so similar and difficult to distinguish, which means that a certain test sample would belong to several circuit modes. So only from a single dimensional array of circuit parameters, the diagnosis result may be unreliable. To solve this problem, a multi-frequency-based information fusion approach is applied in this paper.

Without loss of generality, the total number of the frequency sampling points  $P$  can be expressed in (15), where  $W$  and  $F$  are

respectively the frequency bandwidth and scanning step. For a typical AM-EAS system, signals within the frequency range of 55.5 kHz ~ 60.5 kHz will be handled by the band-pass filter of the receiving circuits. Specifically, if the frequency step is set as 50 Hz, the total number  $P$  equals 100.

$$P = W(\text{Hz}) / F(\text{Hz}) = \frac{W}{F} \quad (15)$$

Then the circuit similarity matrix of the  $TS$  to circuit modes is defined as

$$\Gamma = [e_{i1}, e_{i2}, \dots, e_{ip}], i = 1, \dots, M, k = 1, \dots, P \quad (16)$$

where  $\varepsilon_{ik}$  is circuit similarity matrix under multi-frequency inputs,  $M$  and  $P$  are respectively the totalities of circuit modes and the selected frequency points. Furthermore, we assume that the reliability of different input with different frequency is

$$w = (w_1, \dots, w_p)^T \quad (17)$$

Then the final similarity matrix of the  $TS$  to circuit modes can be rewritten as

$$e = \Gamma \times w = [e_1, e_2, \dots, e_M]^T \quad (18)$$

where,

$$e_i = \sum_{k=1}^P e_{ik} w_k, i = 1, \dots, M \quad (19)$$

Based on the circuit similarity  $\varepsilon_i$  defined in (14),  $\varepsilon_i$  in (19) represents the final similarity of the test sample  $TS$  to the  $i^{\text{th}}$  circuit mode under information fusion of  $N$  circuit parameters and  $P$  frequency responses.

According to literature [9],  $\omega_k$  ( $k=1, \dots, P$ ) in (17) can be computed by the method as below,

$$w_k = a_k b_k / \sum_{k=1}^P a_k b_k, a_k = \max_{i=1}^M \{e_{ik}\}, b_k = a_k / \sum_{i=1}^M e_{ik} \quad (20)$$

The larger the final similarity, the higher the probability that the corresponding component is the faulty one. Then we define the maximum final similarity, the second final maximum similarity and the average value of final similarity matrix as  $\varepsilon_{max1}$ ,  $\varepsilon_{max2}$  and  $\varepsilon_{avg}$  respectively. Finally, the rules for fault location is defined in accordance with the following regulations.

The fault component is the one possessing the maximum final similarity if

- (a)  $\varepsilon_{max1}$  is more than threshold  $\delta$  and
  - (b) the difference between  $\varepsilon_{max1}$  and  $\varepsilon_{max2}$  is more than threshold  $\sigma$ .
- if (a) and (b) are not met, then if
- (c) the ratio between  $\varepsilon_{max1}$  and  $\varepsilon_{avg}$  is more than  $\lambda$ .

The fuzziness of two or more components results mainly from the fact that they take up the same maximum final similarities, which makes the decision rules not work. As we have adopted the two-dimensional information fusion technique (based on  $N$  circuit parameters responding to  $P$  frequency points), the fuzziness is decreased to a large extent.

### III. PROTOTYPE STRUCTURE DESIGN

According to the foregoing analysis, we aim to set up an AFDD prototype with high adaptability in this section. The

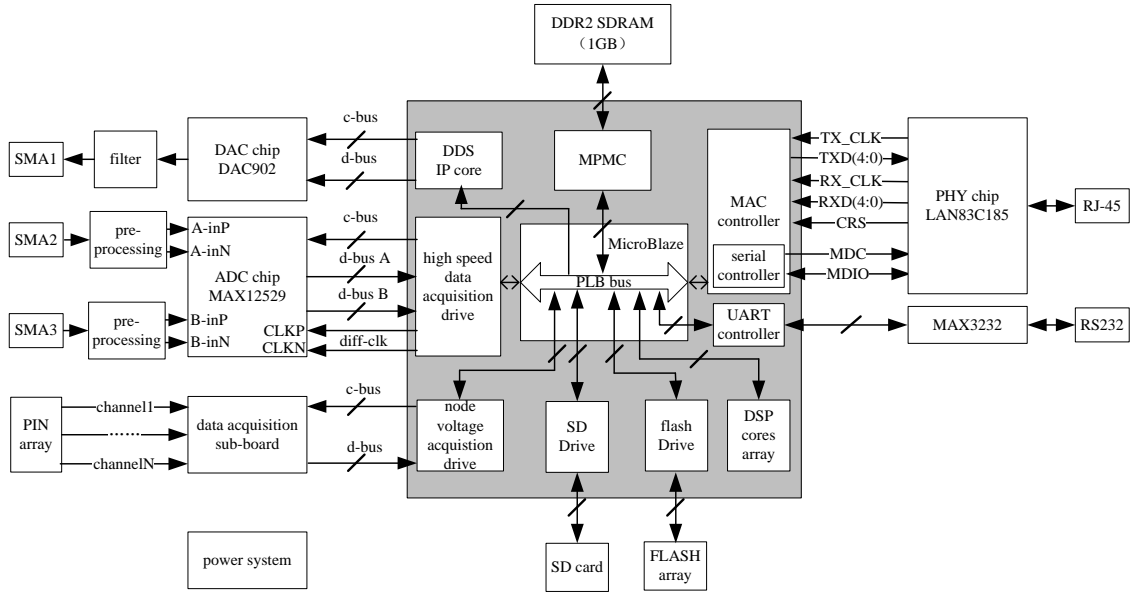


Fig. 2. Topology structure of the proposed analog fault detection and diagnosis system.

It is organized according to the direction of signal flow (which is from left to right), and all the modules in the dotted grey box are implemented in FPGA chip. The interfaces of SMA1, SMA2 and SMA3 correspond to the DAC, ADC1 and ADC2 ports defined in Fig.1, respectively.

proposed hardware scheme is shown in Fig. 2, the chip model of the processor is XC3SD3400A (belongs to Spartan-3A DSP series, Xilinx Inc.). The signal generation part consists of the digital to analog converter (DAC902, 165Mps/12-Bit) and the direct digital synthesizer (DDS) IP core. Then, the frequency sweep signal can be generated from SAM1 port, playing a role of the excitation signal source for CUTs. When it comes to the data acquisition part, there are two different signal objects. For small AC signals, the selected MAX12529 is a dual channel signal acquisition chip having high-performance up to 96Mps/12-Bit. Hence the input/output signals of a certain sub-CUT can be captured by this system through SMA2 and SAM3 simultaneously. For DC signals, in order to simplify design and enhance the flexibility, an extendible sub-board is developed and node voltages can be imported via the PIN array interface conveniently. As for the DSP cores array, it is the computing center of diagnosis algorithms and mainly composed of advanced DSP48E slices, look-up tables (LUTs), true dual-port RAM blocks, first input first output (FIFOs) and share memories. Engineers can reconfigure it flexibly for their specific purpose. At the same time, the system is integrated with sufficient double data rate 2 synchronous dynamic random access memory (DDR2-SDRAM) and flash memory, which support data cache for diagnostic algorithms and backup of intermediate variables. What is more, the raw captured data and analysis results can be transmitted to host server via Ethernet for subsequent processing if necessary. Another significant technology worthy of being emphasized is that all the intellectual property (IP) cores are managed by MicroBlaze (a 32-bit embedded software processor) via processor local bus (PLB). As a prototype, it provides some redundant functions, while in the final engineering applications, the whole scheme should be tailored according to the specific nature of the CUT. And the realized diagnosis platform is given in Fig. 3.

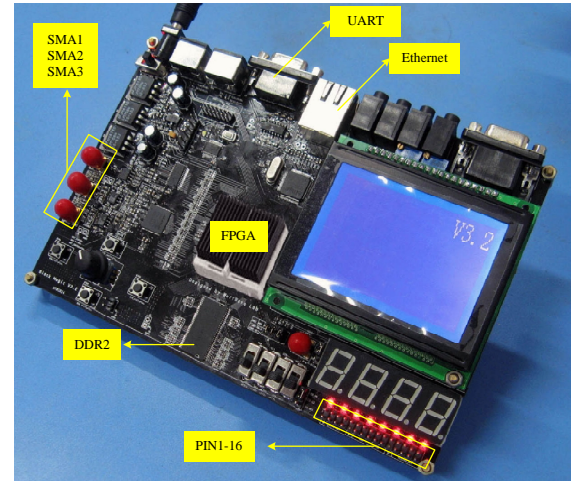


Fig. 3. The FPGA-based diagnosis platform.

#### IV. ILLUSTRATIVE CIRCUITS AND FAULTS

A typical ECB of AM-EAS detection system consists of power supply, transmitter, receiver and DSP controller, where only controller part belongs to digital circuit, the other three are AMS circuits. At present, the popular EAS device has self diagnostic function for its transmitter relying on over-current and over-temperature techniques. Consequently, the following two CUTs mainly focus on power supply and receiver parts, including a switching mode power supply (SMPS) and a multi-stage band-pass filter (BPF). The resistors and capacitors have tolerance values of 1% and 5%, respectively. These two examples illustrate the method for the extraction of feature parameters and the fault diagnosis technique of AMS circuits developed in the previous sections, and we assume that there is an independent relationship between the considered faults for avoiding virtually unlimited testing clusters [10].



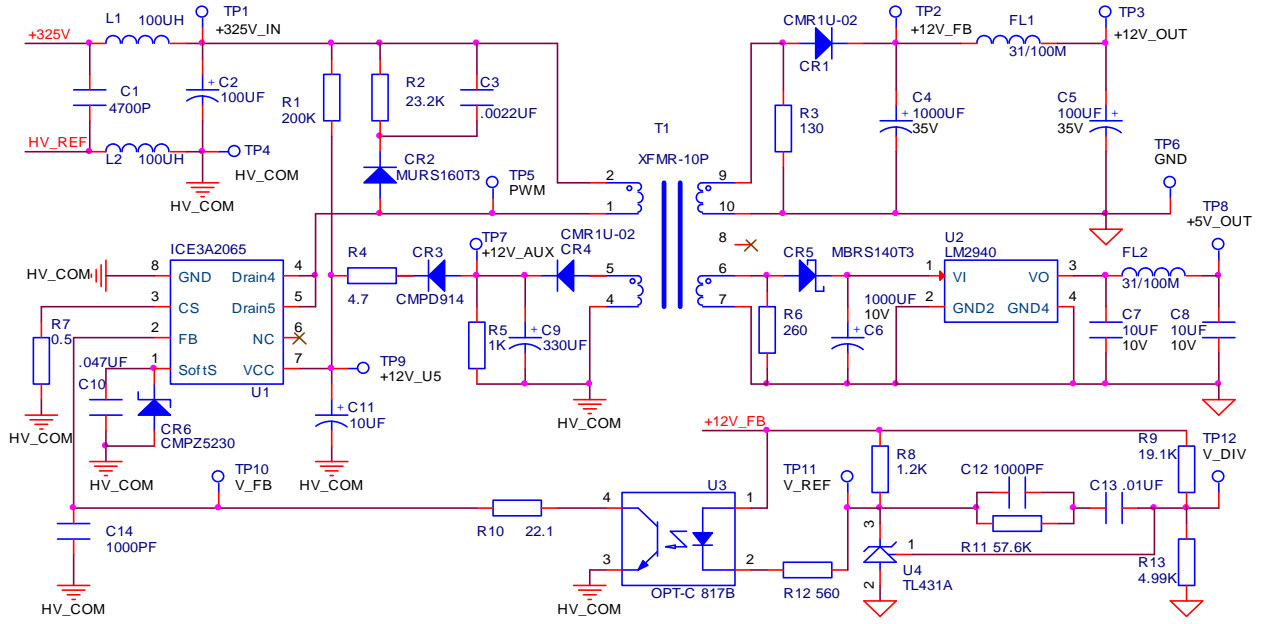


Fig. 4. Example 1: PWM-based SMPS circuit used in this paper.

#### A. Example 1: Switching mode power supply (SMPS)

The SMPS circuit, being the significant precondition of normal working to the whole ECB, is mainly composed of pulse-width modulation (PWM) controller (U1), isolation transformer (T1), three nonlinear half-wave rectifier units (CR1 and C4, CR4 and C9, CR5 and C6) and feedback sub-circuit (centred on U3, U4). The nominal values and chip models for the components are shown in Fig. 4. We will study the availability of our method for nonlinear circuits suffered with hard and soft faults. The considered fault classes include the hard faults caused by open- or short-circuiting C4 ~ C9, C14, CR1, CR4 and CR5 and the soft faults caused by changing the value ratio of R9 and R13 from their correct 3.83 to erroneous 1 or 5.

Among the signals on all the accessible test points from TP1 to TP12, only that on TP5 is an AC signal which is the PWM output wave generated by U1, the remaining are DC level signals. Hence, we will extract the actual signals using input terminals (refer to Fig. 2) of SMA2 and PIN array respectively for data on TP5 and those on the others. As this circuit is not a typical two-port network and mainly related to DC-levels, multi-frequency fusing method has not yet been activated. To sum up, the discussed totalities of circuit modes  $M$  and parameters  $N$  equal 14 and 12, respectively, and that of frequency responses  $P$  is set to the reserved 1. Special emphasis to the test setup on this CUT is that, there are two ground planes isolated by T1, any short-circuiting is not allowed throughout the testing process, so we have equipped corresponding electrical isolation circuits to the pre-processing hardware parts in the proposed AFDD platform.

Then, the feature interval vectors  $FI$  and decision thresholds  $\delta$ ,  $\sigma$ ,  $\lambda$  are trained on PSpice platform through Monte-Carlo simulations for several certain times. In our

design, we compute the “interval similarity”  $\varepsilon$  in (12) through around 1000 times of training. The simulations can also be verified on our realized AFDD system by changing the considered component values on the CUT. Limited by the engineering feasibility, the actual check of the trained values can only be performed in the form of sampling. The final values of  $FI$ ,  $\delta$ ,  $\sigma$  and  $\lambda$  can not be programmed on FLASH ROM until the requirement that true-positive rate (TPR) is no less than 95% is met.

#### B. Example 2: Quad-opamp 4<sup>th</sup> order band-pass filter (BPF)

A flagship AM-EAS system commonly supports 4 transmit-receive channels such as Ultra Exit Series reported in [7]. We firstly partition the receiver into several functional sub-modules trying to find the meta-circuit for case study in Fig. 5a. The signal outputs of the first stage amplifiers are fed into a cross-point switch which allows the signals to be routed to four later amplifier channels in a variety of combinations. Such logic circuitry part is handled through digital method which is beyond the discussion scope in this paper. So we select a representative AMS meta-circuit as the second test example and is shown in Fig. 5b, this is a quad-operational-amplifier (opamp) 4<sup>th</sup> order BPF circuit with programmable pre- and post- amplifiers, and its center frequency and bandwidth are respectively 58 kHz and 5kHz.

In order to simplify the circuit parameter vectors, this test should not be started until the power supply test is passed. In other words, this test is undergoing with normal power supplies on the nets of +5V, +3.3V and +1.6V\_BIAS. The controlling level signals on test points of D33 and D34 are fed into PIN array on the FPGA-based platform for obtaining the gain of the relevant amplifiers. As for the small AC signals, sinusoidal excitation signals sweeping with a 250 Hz step varying from 55.5 kHz to 60.5 kHz are input via the test point A17 (shown in Fig. 5a) to this CUT.

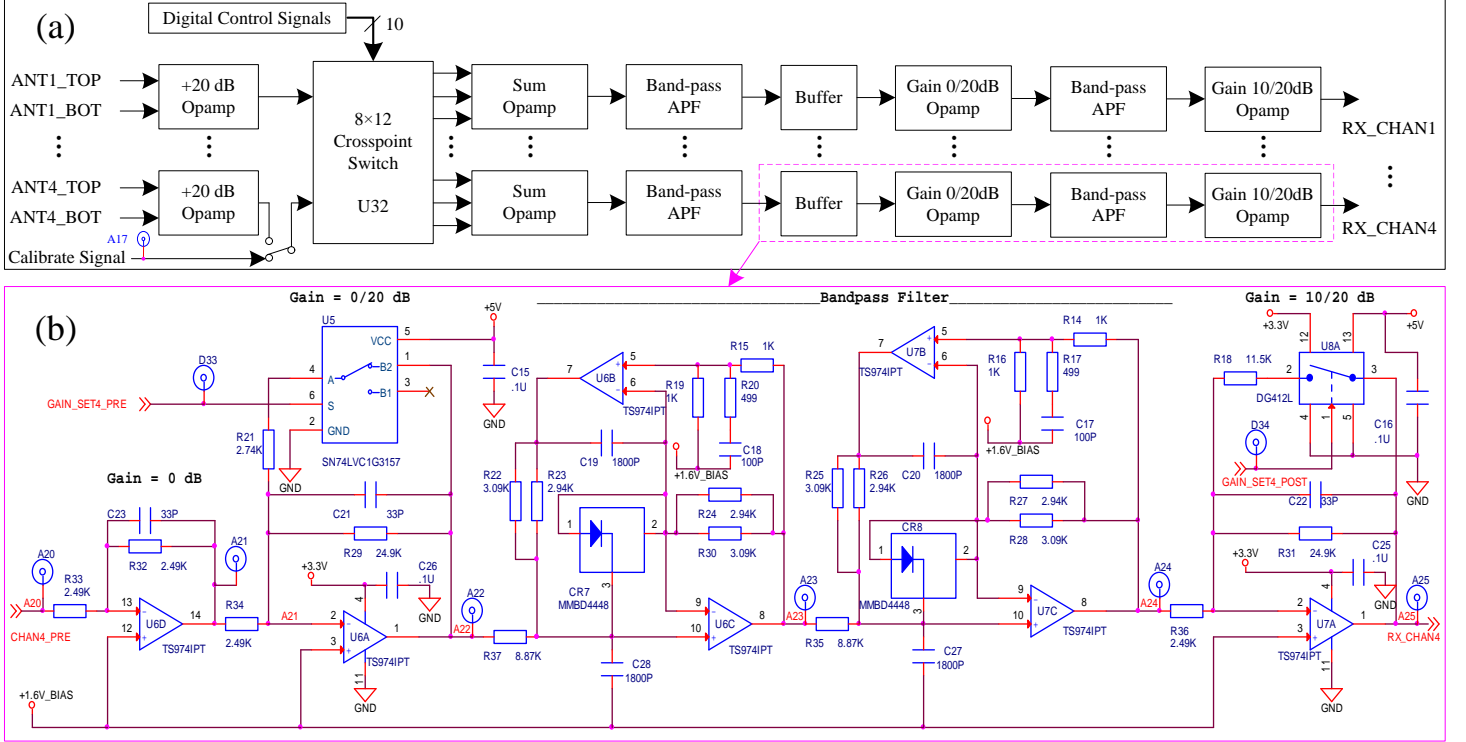


Fig. 5. Example 2: The quad-opamp 4<sup>th</sup> order BPF circuit used in this paper. (a) Receiver circuit structure, and (b) Meta-circuit for case study.

Afterwards, we developed a simple MUX circuit integrated on the ECB under test, to support the rotational scanning on the total 6 intermediate signals on test points of A20 ~ A25. These signals are transmitted to the two output test points A26 and A27 alternately, which can then be fed into the cost-limited data acquisition hardware via SAM2 and SMA3 on the proposed prototype. Fig. 6 gives the relevant MUX circuit part for this considered CUT.

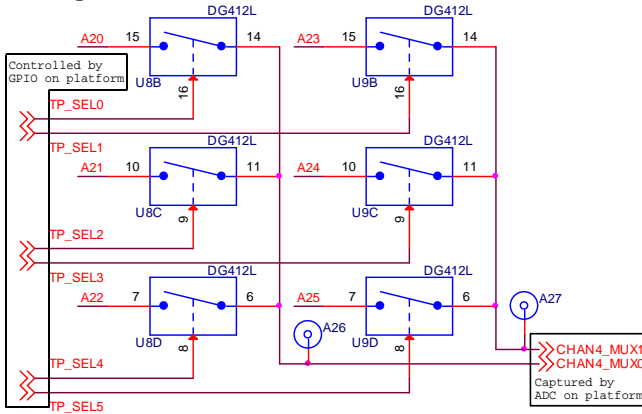


Fig. 6. Test signal multiplexer (MUX).

The fault classes taken as examples include R34  $\uparrow$ , R34  $\downarrow$ , R21  $\uparrow$ , R21  $\downarrow$ , R29  $\uparrow$ , R29  $\downarrow$ , C21  $\uparrow$ , C21  $\downarrow$ , R37  $\uparrow$ , R37  $\downarrow$ , R22/R23  $\uparrow$ , R22/R23  $\downarrow$ , C19  $\uparrow$ , C19  $\downarrow$ , C28  $\uparrow$ , C28  $\downarrow$ , R24/R30  $\uparrow$ , R24/R30  $\downarrow$ , R15  $\uparrow$ , R15  $\downarrow$ , R19  $\uparrow$ , R19  $\downarrow$ , CR7 pin1-3 short circuited (Pin1S3), U6 broken, U5 broken, and the normal state, where  $\uparrow$  and  $\downarrow$  imply significantly higher and lower than nominal values by 20%, respectively.

## V. RESULTS AND ANALYSIS

After that the trained values of  $FI$ ,  $\delta$ ,  $\sigma$  and  $\lambda$  have been solidified on the AFDD system, we firstly illustrate the test results about the aforementioned two example CUTs in this section. Then we evaluate their resource and time consumptions. The decision thresholds  $\delta$ ,  $\sigma$  and  $\lambda$  chosen for these two CUTs are equal to 0.82, 0.24 and 1.75, respectively.

### A. Results and discussion

Using the proposed method, we have studied the fault diagnosis of the pure analog circuit in Fig. 4 and the AMS circuit in Fig. 5. The data in Table I are randomly sampled by our AFDD system when a certain fault (C4 open) occurs on the SMPS circuit. It is observed that the average circuit similarity  $\varepsilon_2$  of the  $TS$  to the feature interval  $FI_2$  based on the 12 circuit parameters ranks first, being bigger than the threshold  $\delta$  (0.82), and there is a safe distance between the threshold  $\sigma$  (0.18) and the difference (0.3262) of  $\varepsilon_{max1}$  and  $\varepsilon_{max2}$ , which mean this fault can uniquely be identified. The false touches to the threshold  $\delta$  which are emphasized with bold fonts appear occasionally under some certain circuit parameters, nevertheless, the final decision-making will not be affected owing to the 12-circuit-parameter fusion. The fault classes and ambiguity groups of SMPS circuit in Fig. 4 are illustrated in Fig. 7, which were obtained by  $50 \times 14$  times of Monte-Carlo analysis for each fault. These results show that nearly all the 14 (including normal) fault classes in the SMPS circuit are falling into different ambiguity groups, and thus, the true-positive rate (TPR) about this CUT is close to 100%. We have been continuously verifying this figure on our actual platform for more than half a year.

TABLE I

FEATURE VALUES FOR HARD-FAULT-DOMINANT CLASSES OF THE NONLINEAR SMPS CIRCUIT, WHEN TS ACCESSES F2

Fault Code: $F_i$	Component	Interval Similarity													
		$\varepsilon_{i1}$	$\varepsilon_{i2}$	$\varepsilon_{i3}$	$\varepsilon_{i4}$	$\varepsilon_{i5}$	$\varepsilon_{i6}$	$\varepsilon_{i7}$	$\varepsilon_{i8}$	$\varepsilon_{i9}$	$\varepsilon_{i10}$	$\varepsilon_{i11}$	$\varepsilon_{i12}$	$\varepsilon_i$	
F1	Normal	0.2608	0.0418	0.0077	0.2740	0.0163	0.2410	0.2920	0.2993	0.2657	0.2591	0.1722	0.2357	0.1971	← TS
F2	C4 open	0.5887	<b>0.9999</b>	<b>0.9989</b>	0.4762	<b>0.9734</b>	<b>0.9466</b>	<b>0.9857</b>	<b>0.9744</b>	<b>0.9676</b>	<b>0.9980</b>	<b>0.9658</b>	<b>0.9952</b>	<b>0.9059</b>	
F3	C5 short	0.2090	0.7094	<b>0.9362</b>	0.1194	0.6072	0.4502	0.4588	0.6620	0.7702	0.3502	0.6620	0.4162	0.5292	
F4	C6 short	0.4088	0.1955	0.0531	0.4915	0.3346	0.1131	0.4399	0.3499	0.3055	0.4789	0.0034	0.3609	0.2946	
F5	C7 short	0.3612	0.4157	0.1862	0.1508	0.0952	0.1923	0.4089	0.3192	0.3894	0.1204	0.3011	0.2367	0.2648	
F6	C8 short	0.0750	0.4017	0.0990	0.3505	0.1845	0.2915	0.1303	0.0168	0.2117	0.3381	0.1934	0.0764	0.1974	
F7	C9 open	0.3298	0.0302	0.2449	0.3332	0.2304	0.1259	0.2972	0.0344	0.0454	0.1446	0.4580	0.1706	0.2037	
F8	C14 short	0.2593	0.1996	0.1698	0.2696	0.4908	0.1452	0.0113	0.1598	0.1333	0.3359	0.0006	0.3037	0.2066	
F9	CR1 short	0.4865	0.2635	0.4758	0.3491	0.0782	0.3085	0.2127	0.2655	0.0769	0.3476	0.2312	0.0959	0.2660	
F10	CR4 short	0.3245	0.2084	0.4602	0.3332	0.4278	0.1326	0.1563	0.3272	0.1405	0.0340	0.2122	0.3692	0.2605	
F11	CR5 short	0.4002	0.3285	0.0263	0.0891	0.3224	0.4122	0.0808	0.2038	0.2201	0.1274	0.2304	0.1214	0.2136	
F12	C14 short	0.2269	0.3140	0.3690	0.0640	0.1882	0.4914	0.0894	0.4100	0.2636	0.1120	0.3851	0.4587	0.2810	
F13	R9/R13=1	0.3243	0.2190	0.2019	0.7492	0.1431	0.5476	0.3172	0.5388	0.3430	0.5009	0.2420	<b>0.8319</b>	0.4132	
F14	R9/R13=5	<b>0.8254</b>	0.4316	0.4228	0.1712	0.4284	0.3438	0.0942	<b>0.9686</b>	<b>0.8754</b>	<b>0.8444</b>	0.7846	0.7654	0.5797	

The fault recognition aiming at the BPF circuit in Fig. 5 is based on the  $2 \times 3$  circuit parameters acquired under 20 equi-spaced frequency points. In order to simplify the description, Table II demonstrates the obtained figures when TS visits F14 category at the center frequency point of 58 kHz. The A-F and P-F parameters captured from the three test points (A21, A22 and A23) have been merged, so the size of the average circuit similarity  $\varepsilon$  in Table II equals  $1 \times 3$ . During this test, although the  $\varepsilon_{14}$  has taken up the maximum value and also exceeds the threshold  $\delta$  (0.82), the final decision-making still seems fuzzy due to the fact that the judging criteria of (b) and (c) defined in Sec. II.B.c are not met. This phenomenon mainly stems from the fact that, some of the Monte-Carlo-analyzed data are overlapped to each other when C19  $\downarrow$  (F14) and R22/R23  $\downarrow$  (F12). For this reason, we need further more information at different frequency points in the bandwidth of the BPF to depress such ambiguous effect. Accordingly, Fig. 8 illustrates the fault classes and ambiguity groups of this CUT by  $50 \times 26$  times of training. It can be clearly learnt that, mainly based on the judging thresholds of  $\delta$  and  $\sigma$ , most of the 26 (including normal) fault classes about the BPF circuit are falling into different ambiguity groups, except a few of test samples touching or crossing their respective lower thresholds. Fortunately, quite a large part of them have been remedied by the reserved criterion of (c). It is also observed that faults occurring on the BPF circuit are more difficult to be diagnosed than that in the proportional opamp circuit, while the diagnostic performance on the capacitors is slightly lower than that on resistors, and the diagnostic

results on chips of U5 and U6 have satisfied the expectations. It is worth mentioning that our method only detects whether the chip is good or bad, but does not continue to analyze the further cause or degree of its deterioration. For the manufacturing and servicing of the large-scale AMS circuits, locating then replacing the defective components is much wiser than sacrificing more cost on the potential reasons. Because the cost of component itself is far lower than that of all-around testing, especially to chips of this kind.

In order to analyze the noise suppression performance of our proposed method, the normal sinusoidal signals carrying random noises (0.01 ~ 0.3) form the final testing excitations, these composite signals are fed into the CUT via A17 in Fig. 5a. The detection performance suffered with this kind of noises is shown in Fig. 9, which indicates that the performance degradation on the true-positive rate (TPR) is no more than 4 % when the normalized noise is lower than 0.3. This result can be explained as no matter what our data acquisition hardware in Fig. 2 or the sum opamp in Fig. 5a, the equipped circuits of differential-signal can suppress the common mode noises to a large extent.

Applying the evaluating terminologies in [11], Table III summarizes the true-positive rate (TPR), false-positive rate (FPR) and false-negative rate (FNR) when considering the normal environment noise level is around 0.1. For the DC-signal circuit like that in Fig. 4, considerable results can be achieved through using only node voltages. For small signal circuits, the detection results show that our proposed two-dimensional fusion method has increased the diagnosis TPR greatly more than that based on a single dimension, which is better than 95%.



TABLE II

FEATURE VALUES FOR SOFT-FAULT-DOMINANT CLASSES OF THE BPF CIRCUIT, CAPTURED AT 58 KHz FREQUENCY POINT, WHEN TS ACCESSES F16

Fault Code: $F_i$	Component	Interval Similarity				Fault Code: $F_i$	Component	Interval Similarity				
		$\varepsilon_{i1}$	$\varepsilon_{i2}$	$\varepsilon_{i3}$	$\varepsilon_i$			$\varepsilon_{i1}$	$\varepsilon_{i2}$	$\varepsilon_{i3}$	$\varepsilon_i$	
F1	R34 $\uparrow$	0.0184	0.2477	0.2716	0.1792	F14	C19 $\downarrow$	0.5909	<b>0.8902</b>	<b>0.9982</b>	<b>0.8264</b>	← TS
F2	R34 $\downarrow$	0.0542	0.1307	0.3019	0.1623	F15	C28 $\uparrow$	0.1824	0.1462	0.2668	0.1985	
F3	R21 $\uparrow$	0.0397	0.2185	0.0423	0.1002	F16	C28 $\downarrow$	0.1618	0.0115	0.3198	0.1644	
F4	R21 $\downarrow$	0.1661	0.0571	0.3045	0.1759	F17	R24//R30 $\uparrow$	0.0498	0.2552	0.1406	0.1485	
F5	R29 $\uparrow$	0.0108	0.2353	0.3199	0.1887	F18	R24//R30 $\downarrow$	0.0858	0.2651	0.3052	0.2187	
F6	R29 $\downarrow$	0.0325	0.0106	0.1135	0.0522	F19	R15 $\uparrow$	0.1802	0.0623	0.2641	0.1689	
F7	C21 $\uparrow$	0.0928	0.0923	0.1951	0.1267	F20	R15 $\downarrow$	0.0848	0.1633	0.3198	0.1893	
F8	C21 $\downarrow$	0.0746	0.0154	0.1823	0.0908	F21	R19 $\uparrow$	0.0186	0.1485	0.2714	0.1462	
F9	R37 $\uparrow$	0.0505	0.0314	0.3192	0.1337	F22	R19 $\downarrow$	0.0119	0.2154	0.0812	0.1028	
F10	R37 $\downarrow$	0.0851	0.2745	0.3216	0.2271	F23	CR7 Pin1S3	0.0830	0.2365	0.3098	0.2098	
F11	R22//R23 $\uparrow$	0.0525	0.2316	0.1687	0.1509	F24	U5 Broken	0.0107	0.2516	0.3113	0.1912	
F12	R22//R23 $\downarrow$	0.4551	<b>0.8235</b>	<b>0.9649</b>	0.7478	F25	U6 Broken	0.0655	0.0920	0.2262	0.1279	
F13	C19 $\uparrow$	0.0330	0.1057	0.3235	0.1541	F26	Normal	0.0837	0.2266	0.2526	0.1876	

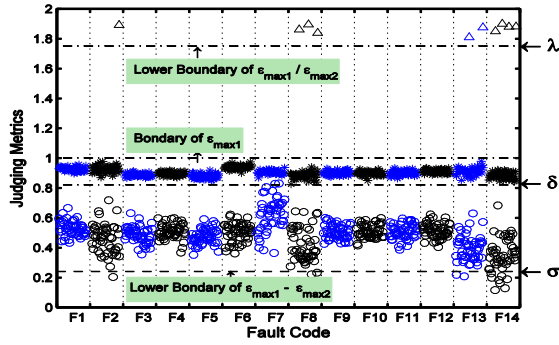


Fig. 7. Fault classes for SMPS circuit in Fig. 4.

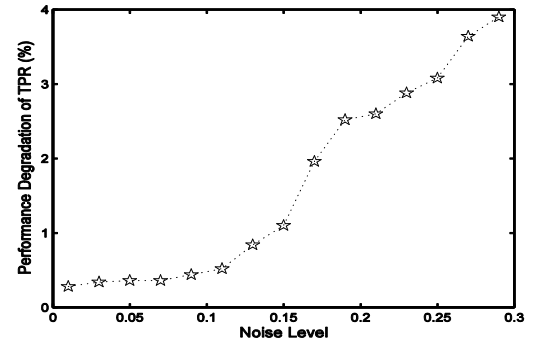


Fig. 9. Performance degradation on the true-positive rate (TPR).

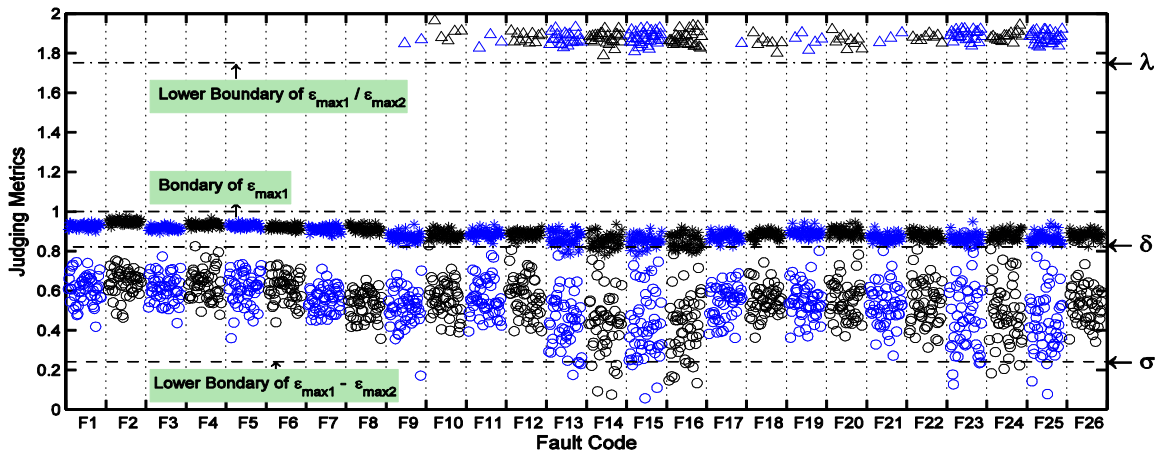


Fig. 8. Fault classes for BPF circuit in Fig. 5.

In addition, the integration level of the DC-signal-circuit (e.g. CUT in Fig. 4) is always slightly lower than that of the small-signal-circuit (e.g. CUT in Fig. 5), so the former kind

of circuit can move more PCB areas for placing test points (accessible nodes), which explains why the parameter totality in Table I equals 12 while that in Table II is only 3.

Such distinguishing method of parameter selection according to different features of circuits possesses higher adaptability for fault diagnosis on VLSI circuits.

### B. Performance evaluation

#### a) Speed

The total time consumption is made up of training time on PC and diagnosis time on FPGA. The training time is mainly spent on the computation of feature intervals and decision thresholds, while nearly nine tenths of the diagnosis time is taken up by the orthogonal algorithm and movements of the calculative data between different memories. The training time on feature intervals and decision thresholds is needed only once on PC while the diagnosis time is repeatedly required in the real applications. Thus, only the later diagnosis time on our embedded platform is considered in the category of real-time analysis.

Table IV gives two kinds of time consumption. It is observed that 3h52m are spent on the parameter training, this result is better than that reported in [12], which we can attribute to the 15 years of development of CPU and memory technology. The trained data are kept in the storage medium on the realized AFDD system for the further fault diagnosis.

TABLE III  
FAULT DIAGNOSIS PERFORMANCE EVALUATION

Diagnosis based on	CUT in Fig. 4			CUT in Fig. 5		
	TPR	FPR	FNR	TPR	FPR	FNR
Node Voltage	96.54	3.46	7.27	57.21	39.65	48.21
A-F	-	-	-	71.28	28.72	9.64
P-F	-	-	-	69.52	30.48	10.19
Fusion	-	-	-	95.78	4.22	2.31

Remark: all the statistical data omit %.

TABLE IV  
TIME CONSUMPTION

CUT in	Parameter	*Total Training Time (s)	** Average Diagnosis Time (s)
Fig.4	Node voltage	1587	0.479
Fig.5		2310	0.984
	A-F	6450	
	P-F	5190	

\*PC: iMac with Intel Core i5-4670 (3.4GHz), 8GB DDR3 memory.

\* Statistical method: use Monte-Carlo analysis with 1000 samples.

\*\*FPGA: XC3SD3400A (200MHz).

\*\*Test method: record the diagnosis time on each considered circuit fault then calculate their average value.

For a specific circuit fault in the example CUTs, the identification result is generated within no more than one second after the hardware setup is finished. Extended to the four receiving channels and all power supplies for transmitter and logic circuits, the total diagnosis time consumption (not including that on hardware set up) is less than one minute. This shows that our developed AFDD system is speedy and effective enough for real applications in the EAS device manufacturing and servicing.

#### b) Resources

As the orthogonal algorithm in the design mainly uses the DSP slices (DSP48As), a large quantity of the Block RAMs have been saved. The utilization summaries of FPGA device and the peripheral resource are illustrated in Table V. Except for the IOBs, the logic usage is less than 10%. As for the peripheral FLASH memory, the example CUTs in the Fig. 4 and Fig. 5 only consume 5.908 KB and 624.000 KB, respectively. Including that of sin-wave-ROM for the DDS IP core, the total FLASH consumption is less than 2%. This means that our implemented system has extendibility for additional processing power, such as the ability to diagnose more complex AMS circuits by fusing more frequency parameters.

TABLE V  
RESOURCE CONSUMPTION

FPGA Device Utilization Summary		
Logic	Utilization(%)	Available
Slice flip flops	4	47,744
4 input look-up tables	6	47,744
Occupied slices	9	23,872
Input/output buffers (IOBs)	29	309
Block RAM Bits	5	2,268K
DSP48As	8	126
Peripheral Resource Utilization Summary		
Item	Utilization(%)	Available
DDR2	5	1GB
FLASH	1.878	32 MB

TABLE VI  
TEST COST COMPARISON

Item	ECB in the Ultra Exit	Our System
PCB Size (mm × mm)	284 × 391	120 × 180
PCB layers	6-layer	4-layer
Power (W)	< 130	< 5
Reference price (USD)	2400	700

## c) Test cost

At present, the frequently-used fault diagnosis method for the AM-EAS devices is based on several instruments including but not limited to arbitrary waveform generator (AWG), oscilloscope (OSC) and high voltage differential probe (HV-DP). In accordance with the requirements of bandwidth, accuracy and channel for an average EAS device, only the instruments would cost more than 3000 USD. Moreover, most of the EAS distributors who are the main liable maintenance deployments to the end retail customers are not familiar with such professional instruments. If there was a smart detection system that can diagnose the AMS fault in real time, this test cost would be dramatically reduced. The detailed cost comparison between the ECB under test and our diagnosis system has been summarized in Table VI. Compared to that in [11], our experimental setup is more compact and practicable to scale to the realistic applications. All of these show promise for the proposed simple detection and diagnosis system to solve the complex AMS circuit faults problems.

## VI. CONCLUSION

This paper has developed a cost-effective fault detection and diagnosis system for AM-EAS devices based on FPGA. The offered abundant acquisition channels are in charge of gathering the circuit parameters of node voltage, amplitude and phase responding to the programmable signal excitations. Test results show that the interval-math-based diagnostic method has three obvious advantages, i.e. resource-saving, fast detecting speed, and balanced statistical rates among TPR, FPR and FNR.

However, because Monte-Carlo simulation is relatively time consuming, we have to spend a fair chunk of time on the training of the feature intervals and the decision thresholds on PC, which are just closely related to the AFDD system's detecting performance. Future research will focus on making the training method more time-saving and the embedded algorithm more efficient, with the goal of portable diagnostic equipment that could stand ready for widespread adoption in the EAS industry.

## REFERENCES

- [1] Y. He, Y.H. Tan and Y. Sun, "A neural network approach for fault diagnosis of large-scale analogue circuits," in *IEEE Int. Symp. on Circuits and Systems (ISCAS)*, May 2002, vol.1, pp.1-153-1-156.
- [2] P. Wang and S.Y. Yang, "A new diagnosis approach for handling tolerance in analog and mixed-signal circuits by using fuzzy math," *IEEE Trans. Circuits Syst. I, Reg. Papers*, vol.52, no.10, pp.2118-2127, Oct. 2005.
- [3] V. Stopjakova et al., "Defect detection in analog and mixed circuits by neural networks using wavelet analysis," *IEEE Trans. Rel.*, vol.54, no.3, pp. 441-448, Sep. 2005.
- [4] P.N. Variyam, S. Cherubal and A. Chatterjee, "Prediction of analog performance parameters using fast transient testing," *IEEE Trans. Comput.-Aided Design Integr. Circuits Syst.*, vol. 21, no. 3, pp. 349-361, Aug. 2002.
- [5] Q. Yang, Y.Y. Zhu and F. Wu, "Remote Intelligent Fault Diagnosis of Analog Circuit," *IEEE Int. Conf. on Natural Comput. (ICNC)*, Shanghai, China, Jul. 2011, vol. 3, pp. 1677-1680.
- [6] G. Kang and Om P. Gandhi, "Comparison of various safety guidelines for electronic article surveillance devices with pulsed magnetic fields," *IEEE Trans. Biomed. Engineering*, vol. 50, no. 1, pp. 107-113, Jan. 2003.
- [7] E. Bottani et al., "Performances of RFID, acousto-magnetic and radio frequency technologies for electronic article surveillance in the apparel industry in Europe: A quantitative study," *I. J. RF Technol.: Res. and Appl.*, vol. 3, no. 2, pp. 137-158, 2012.
- [8] M.F. Peng, Y. He and Y. Sun, "Analog circuit diagnosis using RBF network and D-S evidential reasoning," *Trans. of China Electrotechnical Society*, vol. 24, no.8, pp. 6-13, Aug. 2009.
- [9] M.F. Peng Y. He and J.X. Lv, "Fault location of analog circuits using intelligent information fusion technology (IN CHINESE)," *Trans. of China Electrotechnical Society*, vol. 20, no. 11, pp. 93-96, Nov. 2005.
- [10] L. F. Yuan, Y. He and Y. Sun, "A new neural-network-based fault diagnosis approach for analog circuits by using kurtosis and entropy as a preprocessor," *IEEE Trans. Instrum. Meas.*, vol. 59, no. 3, pp. 586 - 595, Mar. 2010.
- [11] A. S. Sarathi Vasan, B. Long and M. Pecht, "Diagnostics and prognostics method for analog electronic circuits," *IEEE Trans. Ind. Electron.*, vol. 60, no. 11, pp. 5277-5291, Nov. 2013.
- [12] A. Abderrahman, E. Cerny and B. Kaminska, "Worst Case Tolerance Analysis and CLP-Based Multifrequency Test Generation for Analog Circuits," *IEEE Trans. Comput.-Aided Design Integr. Circuits Syst.*, vol. 18, no. 3, pp. 332-345, Mar. 1999.

**Qiwu Luo** received his M.S. degree in Electronic Science and Technology in 2011 and is currently pursuing his Ph.D. degree in Electrical Engineering from Hunan University, Changsha, China. His current interests include the research of fault testing and diagnosis of large-scale analog circuits, intelligent and real-time information processing.

Contact Infor: Room 619, Research Building, College of Electrical and Information Engineering, Hunan University, Yue Lu District, Changsha, Hunan, China.  
Tel: +86(0)731 88822252, Fax: +86(0)731 88822224,  
E-mail: [luoqiwu@hnu.edu.cn](mailto:luoqiwu@hnu.edu.cn)

**Yigang He** is currently a professor of Electrical Engineering at Hefei University of Technology, Hefei, China. He received his Ph.D. degree in electrical engineering from Xi'an Jiaotong University, Xi'an, China, in 1996. His research interests include testing and fault diagnosis of analog and mixed-signal circuits, intelligent signal processing and RFID.

Contact Infor: Floor 11, Yifu Building, School of Electrical and Automation Engineering, Hefei University of Technology, Hefei, Anhui, China.  
Tel: +86(0)551 62904435, Fax: +86(0)551 62901408,  
E-mail: [18655136887@163.com](mailto:18655136887@163.com)

**Yichuang Sun** is currently a professor of Communications Electronics at University of Hertfordshire, UK. He received his Ph.D. degree from University of York, U.K. His research interests are integrated RF and mixed-signal circuits, software defined radio transceivers, and wireless and mobile communication systems. He is a Senior Member of IEEE.

Contact Infor: School of Engineering and Technology, University of Hertfordshire, Hatfield AL10 9AB, Hertfordshire, United Kingdom.  
Tel: +44(0)1707 284196, Fax: +44(0)1707 284199,  
E-mail: [y.sun@herts.ac.uk](mailto:y.sun@herts.ac.uk)